

# Cavitation structures formed during the rebound of a sphere from a wetted surface

J. O. Marston · W. Yong · W. K. Ng ·  
R. B. H. Tan · S. T. Thoroddsen

Received: 19 May 2010/Revised: 27 July 2010/Accepted: 9 September 2010/Published online: 28 September 2010  
© Springer-Verlag 2010

**Abstract** We use high-speed imaging to observe the dynamics of cavitation, caused by the impact and subsequent rebound of a sphere from a solid surface covered with a thin layer of highly viscous liquid. We note marked qualitative differences between the cavitation structures with increase in viscosity, as well as between Newtonian and non-Newtonian liquids. The patterns observed are quite unexpected and intricate, appearing in concentric ring formations around the site of impact. In all cases, we identify a distinct radius from which the primary bubbles emanate. This radius is modelled with a modified form of Hertz contact theory. Within this radius, we show that some fine cavitation structure may exist or that it may be one large cavitation bubble. For the non-Newtonian fluids, we observe foam-like structures extending radially with diminishing bubble sizes with increase in radial position. Whereas for the Newtonian fluids, the opposite trend is observed with increasing bubble size for increasing radial position. Finally, we compare our experimental

observations of cavitation to the *maximum tension criterion* proposed by Joseph (J Fluid Mech 366:367–378, 1998) showing that this provides the lower limit for the onset of cavitation in our experiments.

## 1 Introduction

The collision of two solids is a fundamental occurrence in nature and industry. When two colliding surfaces are wet or partially wet, as may be witnessed in granulation for example (Salman et al. 2006), a basic piece of information is the outcome of that collision. That is, will the surfaces stick or rebound? Example sequences showing the outcomes of three different collisions—namely—rebound from a low-viscosity film, sticking onto a high-viscosity film and rebound from a high-viscosity film are shown in Fig. 1. In these sequences, all taken from high-speed video clips at 20 kfps, a steel sphere impacts a glass base target covered with a thin layer of viscous liquid (see caption for impact conditions). In Fig. 1a, for the low-viscosity liquid, the sphere is partially wetted during impact and the contact line remains pinned on the sphere surface so that a liquid bridge is formed during the initial stages of rebound. At the extreme opposite, Fig. 1b shows a low-inertia impact onto a high-viscosity film and the particle motion is completely arrested by the film. In contrast, Fig. 1c, for a high impact velocity onto an ultra-high viscosity film shows rebound where the liquid bridge “snaps” in the early stages of rebound, likely due to the effect of cavitation. This fundamental observation was a key motivation for this research. Following from Barnocky and Davis (1988), we suspect that cavitation also occurs in Fig. 1a for the rebound from the low-viscosity film, but this cannot be seen from the side perspective shown.

**Electronic supplementary material** The online version of this article (doi:10.1007/s00348-010-0979-9) contains supplementary material, which is available to authorized users.

J. O. Marston · W. K. Ng · R. B. H. Tan  
A-STAR Institute of Chemical and Engineering Sciences,  
1 Pesek Road, Jurong Island, Singapore 627833, Singapore

W. Yong · R. B. H. Tan  
Department of Chemical and Biomolecular Engineering,  
National University of Singapore, 4 Engineering Drive 4,  
Singapore 117576, Singapore

J. O. Marston (✉) · S. T. Thoroddsen  
Division of Physical Sciences and Engineering,  
King Abdullah University of Science and Technology,  
Thuwal 23955-6900, Saudi Arabia  
e-mail: jeremy.marston@kaust.edu.sa

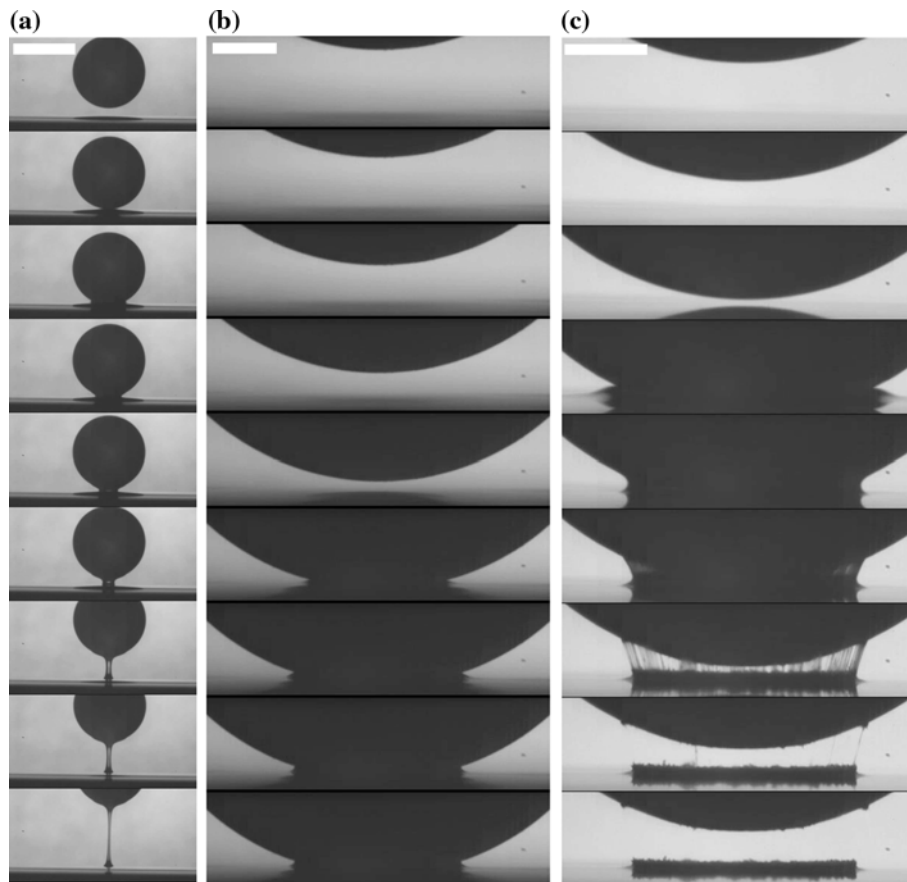


**Fig. 1** **a** Rebound from low-viscosity film ( $St = 12.3$ ,  $\epsilon = 1.21 \times 10^{-6}$ ,  $\delta = 350 \mu\text{m}$ ), **b** Sticking in high-viscosity film ( $St = 0.063$ ,  $\epsilon = 0.0039$ ,  $\delta = 175 \mu\text{m}$ ), **c** Rebound from an ultra-high viscosity film ( $St = 0.0172$ ,  $\epsilon = 0.0197$ ,  $\delta = 350 \mu\text{m}$ ). Cavitation is the cause of the liquid bridge snapping in **c** and is also suspected to occur

in **a**. The scale bars in each indicate 2 mm and the time of the frames shown relative to impact are **a**  $-0.5, 0, 0.3, 0.5, 1.3, 2.3, 3.3, 4.3, 8.3$  ms, **b**  $-4.5, -3.5, -2.5, -1.5, -0.5, 0.5, 1.0, 2.5, 3.5$  ms and **c**  $-1.1, -0.6, -0.1, 0.5, 1.0, 1.5, 2.0, 2.4, 2.9$  ms. The Stated values of the Stokes' number are based on the low shear viscosities,  $\mu_0$

The elastohydrodynamic rebound problem has been studied rather intensively since the pioneering work of Davis et al. (1986) who derived the theory for the relative motion of two colliding spheres separated by a viscous liquid, showing that the important parameters governing the rebound are an elasticity parameter,  $\epsilon$ , incorporating the mechanical properties of the solids, and a Stokes number,  $St$ , measuring the inertia of the colliding spheres relative to viscous forces in the thin layer. These two parameters are given by

$$\epsilon = \frac{4\theta\mu v_0 a^{3/2}}{x_0^{5/2}}, \quad St = \frac{\rho_s D v_0}{9\mu} \tag{1}$$

where  $\theta = (1 - \nu_1^2)/\pi E_1 + (1 - \nu_2^2)/\pi E_2$ , where  $\nu_1$  and  $\nu_2$  are the Poisson's ratios of the sphere and plane, and  $E_1$  and  $E_2$  are the Young's modulus of the sphere and plane,  $\mu$  is the liquid dynamic viscosity,  $v_0$  is the sphere velocity at the initial separation  $x_0$ ,  $a = D/2$  is the sphere radius (for sphere-wall collisions only),  $D$  is the sphere diameter and  $\rho_s$  is the sphere density.

Davis et al. (2002) extended this theory to look at spheres impacting a planar wall, where it was deduced that a sphere impacting a wall covered with a thin layer of viscous liquid will rebound once the impact velocity reaches a critical value. When this threshold velocity is exceeded, the lubrication force, which arises due to the fluid being squeezed out from between the surfaces, becomes strong enough to deform the sphere. Thus, rebound occurs as the elastic strain energy stored is converted back to kinetic energy. This solid deformation is expected to occur once the sphere has penetrated sufficiently far into the liquid so that the separation between the sphere and the wall,  $x$ , is equivalent to an elasticity lengthscale (Davis et al. 2002)

$$x_r = (3\pi\theta\mu a^{3/2} v_0 / \sqrt{2})^{2/5}, \tag{2}$$

This scaling only holds if it is assumed that the sphere retains half of its initial velocity, that is  $v = v_0/2$  at  $x \sim x_r$ . Note that this assumption was introduced in the analysis of Davis et al. (2002) so that an analytical solution could be

found and that  $x_r$  could be written explicitly. Recent work by Marston et al. (2010) puts this approximation on more solid ground with direct experimental measurements of the deceleration of the sphere within the thin film, giving results of the same order of magnitude.

At this point, the direction of motion is reversed and the sphere rebounds from the wall. In reference to the stress in the liquid induced by the separation of the solids during rebound, Barnocky and Davis (1988) and Davis et al. (2002) state that “Since the fluid easily cavitates at these high tensile stresses, the resistance to the motion is small relative to the resistance during approach and thus is neglected.”

The theory of Davis et al. (1986) has been used several times in subsequent works such as non-normal collisions (e.g. Kantak and Davis 2004) and recent developments in multi-particle collisions (Kantak et al. 2009; Donahue et al. 2010). Donahue et al. (2010) incorporate the so-called ‘glass-transition’ into their analysis whereby the oils used in the experiments undergo a transition from liquid to solid-like behaviour which may benefit the rebound. Ardakani et al. (2009) present the first experimental measurements of impact–rebound velocities in non-Newtonian systems showing distinct differences from the Newtonian case, especially when analysed in terms of a Deborah number based on the particle impact velocity.

More specific to the work presented in this paper, Joseph (1998) provides a comprehensive review of the criterion for cavitation to occur and, for the case of surfaces separating in a liquid, cavitation is expected when the tensile stress in the liquid exceeds one atmosphere of pressure. Some experimental efforts are cited therein (e.g. Kuhl et al. 1994). Other recent observations of cavitation between a rolling sphere and a curved wall in lubrication flow have been reported by Ashmore et al. (2005), Prokunin and Slavin (2006), Yang et al. (2006) and by Seddon and Mullin (2008) who note a spherical cavity for a Newtonian liquid but “several tongues” of fluid stretched across the cavitation site for a visco-elastic Boger fluid.

However, to our knowledge, the work herein provides the first detailed imaging of the quite unexpected and intricate cavitation formed during the separation of two surfaces at high-speed in both Newtonian and non-Newtonian liquids. We provide a qualitative description of the features of the cavitation patterns formed during the rebound of a solid sphere which impacts vertically onto a horizontal solid surface covered with a thin layer of viscous liquid, such as the ideal cases considered by Barnocky and Davis (1988) and Davis et al. (2002). This previously unreported phenomenon is shown to exhibit drastic differences between low and high viscosity as well as between Newtonian and non-Newtonian fluids. Our findings also appear to be in accord with previously developed criterion for cavitation.

## 2 Experimental setup and method

The experimental setup used for these experiments is shown in Fig. 2a and b. The impacting sphere is released from an electromagnet secured directly above the target on an aluminium spine rail to allow for a range of release heights,  $1 \text{ cm} < h_r < 34 \text{ cm}$ , to be tested. The spheres are made from stainless steel (Cyclematic Precision Eng. Ltd, Singapore) with diameters,  $D = 38$  and  $50 \text{ mm}$  and density,  $\rho_s \sim 7,850 \text{ kg/m}^3$ . The target base is a glass plate with dimensions  $110 \times 110 \times 19 \text{ mm}$ . For such materials we conclude  $\theta \sim 6.15 \times 10^{-12}$  and  $\epsilon \sim 10^{-5} - 10^{-3}$  (based on parameters used in the experiments). Due to the large spheres used in these experiments, having a solid base is crucial for consistency. As such, the plate is held securely by a solid stainless steel frame with a mass of approximately 6 kg. The frame is a hollow U-shape to accommodate a mirror angled at  $45^\circ$  to enable observations of the underside of the sphere.

The thin liquid films were placed directly onto the glass in a square perimeter fixed to the surface. We focused mainly on a film thickness,  $\delta = 1.5 \text{ mm}$ , for consistency although in preliminary experiments with smaller spheres (e.g. Fig. 1) we used thinner layers ( $\delta = 175\text{--}350 \mu\text{m}$ ) where the liquid was brushed on to the plate. Between

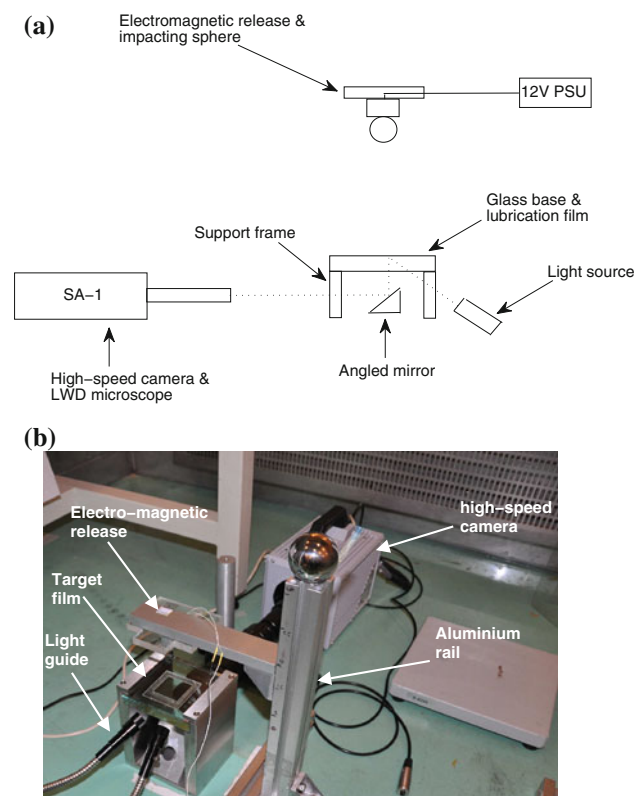


**Fig. 2** **a** Schematic of the experimental facility. **b** Photograph of the experimental facility in the laboratory

**Table 1** Fluid properties used

Fluid	Viscosity, $\mu$ or $\mu_0$ (Pa.s)	Density, $\rho$ (kg/m <sup>3</sup> )	Additional info
Pure glycerol	1.25	1,260	Newtonian
90% syrup	1.6	1,396	Newtonian
95% syrup	8.47	1,418	Newtonian
Pure syrup	32	1,438	Newtonian
12,500 cSt silicone oil <sup>a</sup>	12.13	970	Shear-thinning, compressible
60,000 cSt silicone oil <sup>a</sup>	58.2	970	Shear-thinning, compressible
100,000 cSt silicone oil <sup>b</sup>	97.7	977	Shear-thinning, compressible
1,000,000 cSt silicone oil <sup>b</sup>	978	978	Shear-thinning, compressible

The densities of syrup mixtures are calculated assuming linear mixing and those of the oils are taken from manufacturers' data

<sup>a</sup> Brookfield Engineering Laboratories, Inc.

<sup>b</sup> Shin-Etsu Chemical Co. Ltd.

trials, the sphere was manually removed, cleaned with a water–ethanol mixture and dried with an air gun. The liquid film was routinely replenished between trials and levelled with a microscope slide for the Newtonian liquids with  $\mu < 32$  Pa.s. For the ultra-viscous non-Newtonian liquids, however, several plates were prepared at least 24 hours before the trials to ensure a uniform level was attained.

The physical properties of the liquids used in these experiments are listed in Table 1. For the Newtonian liquids, we used glycerol and mixtures of Tate & Lyle's Golden Syrup (mixed with water) yielding a good range of viscosities with  $\mu = 1.25, 1.6, 8.47$  and  $32$  Pa.s measured (at the ambient lab temperatures) by an Anton Paar MCR301 Rheometer in a concentric cylinder geometry at temperatures from  $20$  to  $25^\circ\text{C}$  in increments of  $0.5^\circ\text{C}$ . For the non-Newtonian liquids we chose (dimethylpolysiloxane) silicone oils (Shin-Etsu Chemical Co. Ltd, Japan) with nominal low shear ( $\dot{\gamma} < 100 \text{ s}^{-1}$ ) kinematic viscosities of  $\nu = 100,000$  cSt ( $\mu_0 = 97.7$  Pa.s) and  $\nu = 1,000,000$  cSt ( $\mu_0 = 978$  Pa.s) (measured at  $25^\circ\text{C}$ ). The data supplied by the manufacturer suggests that these fluids are both compressible and shear-thinning. Following from Marston et al. (2010), the  $\mu_0 = 97.7$  Pa.s oil can be described by the Carreau model,  $(\mu - \mu_\infty)/(\mu_0 - \mu_\infty) = [1 + (\lambda\dot{\gamma})^2]^{(n-1)/2}$  with a zero shear viscosity  $\mu_0 = 97.7$ , infinite shear viscosity  $\mu_\infty = 0$ ,  $\lambda = 4.88 \times 10^{-3}$  s and  $n = 0.455$ . A plot of apparent viscosity versus shear rate for this fluid is presented in Fig. 3.

In addition, 'viscosity standard' oils (Brookfield Engineering Laboratories, Inc.) used in viscometer calibrations with viscosities of  $\nu = 12,500$  cSt ( $\mu_0 = 12.13$  Pa.s) and  $\nu = 60,000$  cSt ( $\mu_0 = 58.2$  Pa.s) were used. However, these fluids have the same chemical structure (i.e. dimethylpolysiloxane) as the Shin-Etsu silicone oils and only exhibit Newtonian behaviour at low shear rates. Under the conditions used in the present experiments, they also exhibit strong non-Newtonian properties as shown by Marston et al. (2010).

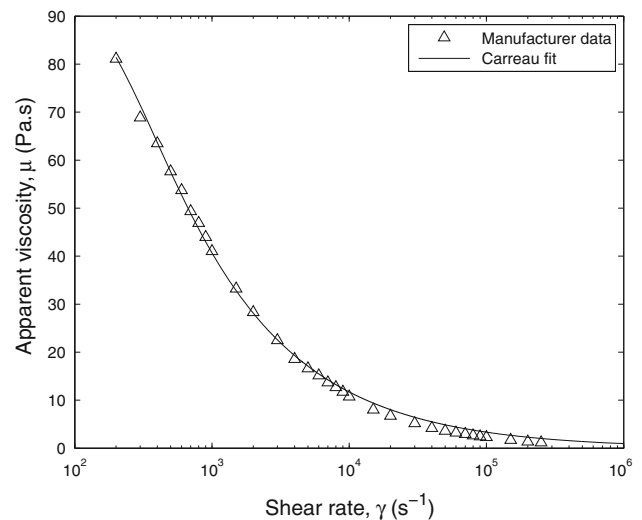


**Fig. 3** Rheological data for 100,000 cSt silicone oil. The data points are taken from the manufacturer's data and the theoretical fit with the Carreau model assumes a zero shear viscosity  $\mu_0 = 97.7$  Pa.s (as stated by the manufacturer). The resulting parameters are  $\mu_\infty = 0$ ,  $\lambda = 4.88 \times 10^{-3}$  and  $n = 0.455$

To minimise temperature fluctuations and moisture absorption, the experiments were carried out in a humidity-controlled chamber with  $\text{RH} = 25\%$  and temperature set to  $20^\circ\text{C}$ . The entire experimental setup was placed directly on the concrete ground floor in order to eliminate any oscillations carried through the apparatus, caused by the impact itself. The events were recorded by a Photron Fastcam SA-1 high-speed camera equipped with a long working distance microscope (Leica Z16) at frames rates up to  $20$  kfps yielding a resolution of at least  $512 \times 512$  pixels and a recording time long enough to allow for manual triggering. Depending on the magnification used, the effective pixel resolution was in the range  $4.2\text{--}17 \mu\text{m}/\text{pixel}$ . The video clips were saved directly to a PC for subsequent image analysis. The lighting was provided by a  $350$  W Sumita metal halide light source equipped with a dual fibre-optic guides which induces minimal heating to the film, as checked by temperature measurements.

### 3 Experimental observations

#### 3.1 Non-Newtonian films

Figure 4 shows the sequence of events for the impact of a stainless steel sphere ( $D = 38$  mm) onto a glass base ( $h = 19$  mm) covered with a thin layer ( $\delta = 1.5$  mm,  $\delta/D = 0.039$ ) of silicone oil with  $\mu_0 = 12.13$  Pa.s. The impact velocity for this instance was  $u_i = 1.33$  m/s and the frames shown are from a clip taken at 20 kfps (see also the supplementary video clip for this figure). The first image (top left) is the last frame before any cavitation is noticed during the rebound stage and is taken as  $t_0$  for reference. The bright spot at the top of each frame is the reflection of the light source. The inception of cavitation bubbles are first identified at  $t = 0.1$  ms by the bright reflections which are from the interfaces between different bubbles. The inception sites advance radially outward from a distinct central radius.

The bubbles appear to decrease in size with increasing radial distance from the centre and assemble in a densely packed structure whereas the rings of bubbles immediately surrounding the central impact site are much larger and discrete. The radial expanse of the cavitation reaches a maximum approximately 1.4 ms (top right image) after first inception and subsequently contracts back towards the centre (see final column) as the sphere separates further from the base surface.

A more detailed snapshot from this sequence (taken at 1.4 ms after  $t_0$ ) is shown in Fig. 5, where the boundary of the discrete central radius can be clearly seen with a contact diameter,  $d_c = 1.9$  mm. The arrow at the top of the image indicates the maximum extent of the cavitation structure, here measured to be  $r_{\max} = 4.5$  mm, or 24% of the sphere radius. As discussed later, we believe the radial location from which bubbles appear to emanate in fact marks the extent of the equivalent Hertzian contact area, i.e. the area of the nose of the sphere which becomes flattened due to elastic deformation during the collision. Upon close inspection inside this radius in Fig. 5, there does appear to be some fine structure which may also be due the cavitation, however due to the small gap width within this region, it is not as clear as the structure outside the contact radius. This suggests that the thin residual liquid film on the sphere and the plate (separated by the fine cavitation) may be of uneven thickness.

Figures 6 (sequence) and 7 (detailed) show an equivalent set of images for a higher viscosity oil with  $\mu_0 = 58.2$  Pa.s, sphere diameter  $D = 38$  mm and impact velocity  $u_i = 1.79$  m/s. For this realisation, the structure reaches maximal radial spread,  $r_{\max} = 5.7$  mm at  $t = 2.2$  ms from  $t_0$ , compared to  $t = 1.4$  ms for Fig. 4. The larger radius of the structure in this case is due to the higher

impact and rebounding velocity. The retraction phase of the structure (seen in the final column) is also slower for this liquid, which is expected due to the increased viscosity of the layer. From Fig. 7, we also find the contact diameter in this case is  $d_c = 2.1$  mm along with more distinct patterns at larger radial positions, as marked by the arrows in Fig. 7.

Similar cavitation structures are also observed when the liquid layer is silicone oil of even higher viscosity, also known to be non-Newtonian. Examples of the intricate structures formed can be seen in Fig. 8 for Shin–Etsu oils with (a)  $\mu_0 = 97.7$  Pa.s (see the supplementary video clip for this figure) and (b)  $\mu_0 = 978$  Pa.s. The radial pattern of gradually diminishing vapour bubbles is again clear from these images. Note the similarity between Figs. 7 and 8a, both with  $D = 38$  mm and  $u_i = 1.79$  m/s, taken at similar times during the retraction phase. Figure 8b for  $\mu_0 = 978$  Pa.s shows an even more striking example of the cavitation structure which extends from a finite radius (central ‘contact’ site) and grows radially outwards in time. This image is from a video sequence taken at 20 kfps for a 50 mm sphere. Again, we see a pattern that changes with increasing radial position. The inner contact area is clearly distinguished with a diameter of 2.5 mm (marked by arrow B). A notable difference between this structure and that in Figs. 5, 7 and 8a is the ring immediately surrounding the contact area; In this realisation there is a ring of elongated bubbles making an ordered ‘sunflower’ pattern before turning into a more densely packed ‘foam-like’ structure of bubbles. This boundary is marked by arrow C. Note also in this case, the central contact area contains a smaller circle marked by arrow A, which appears to confirm our observation in Fig. 5 that some fine cavitation structure does in fact exist within the contact radius.

#### 3.2 Newtonian films

In contrast, for liquids with low viscosity known to be purely Newtonian, we find a qualitatively different cavitation structure induced by the collision process; Fig. 9 (see also the supplementary video clip for this figure) shows a sequence taken for a 50 mm sphere impacting onto a Newtonian film of 95% golden syrup ( $\mu = 8.47$  Pa.s). The two columns in Fig. 9 depict the opening and subsequent collapse of the cavitation structure. The cavitation reaches its maximum extent within the first millisecond of detection and has collapsed after 5.5 ms. The differences between this sequence of images and those of Figs. 4, 5, 6, 7 and 8 for the silicone oils are clear; in the region immediately surrounding the contact area ( $d_c = 2.1$  mm) we find an annulus of fine bubbles, followed by intermediate sized bubbles and a distinct outer region containing macroscopic voids approximately 1.5–2 mm in diameter

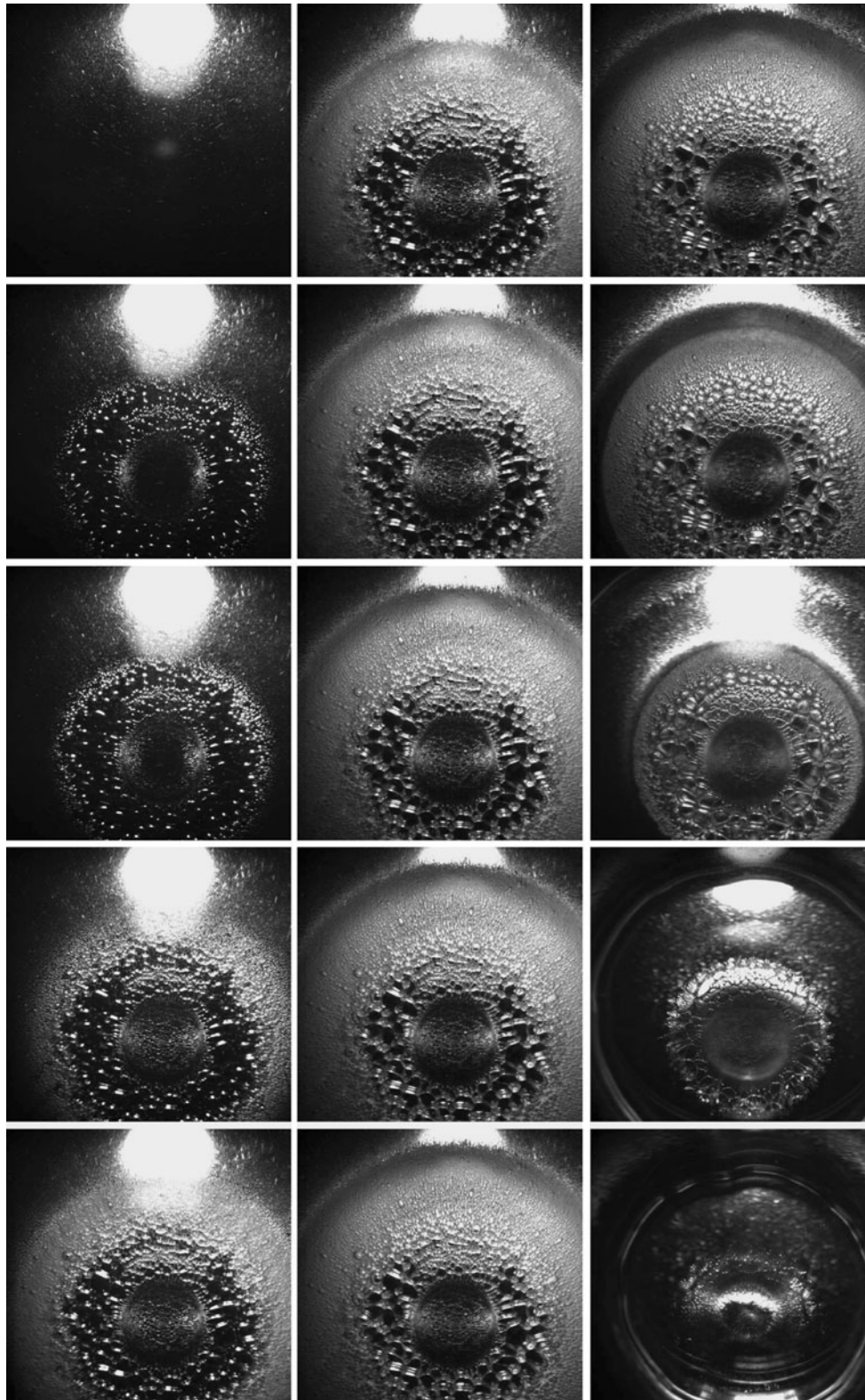


**Fig. 4** Cavitation pattern viewed from below. The *top left* image is the frame before any cavitation bubbles are first seen and thus we take this frame as  $t_0$  for reference. Subsequent frames (*top to bottom and left to right*) are taken at 0.1, 0.2, 0.3, 0.4, 0.5, 0.6, 0.7, 0.8, 0.9, 1.4,

1.9, 2.9, 3.9 and 4.9 ms after  $t_0$ .  $D = 38$  mm,  $\mu_0 = 12.13$  Pa.s,  $\delta = 1.5$  mm and  $u_i = 1.33$  m/s ( $St = 3.67$ ,  $\epsilon = 3.2 \times 10^{-5}$ ). See also supplementary video 1, taken at 20 kfps, accompanying this figure

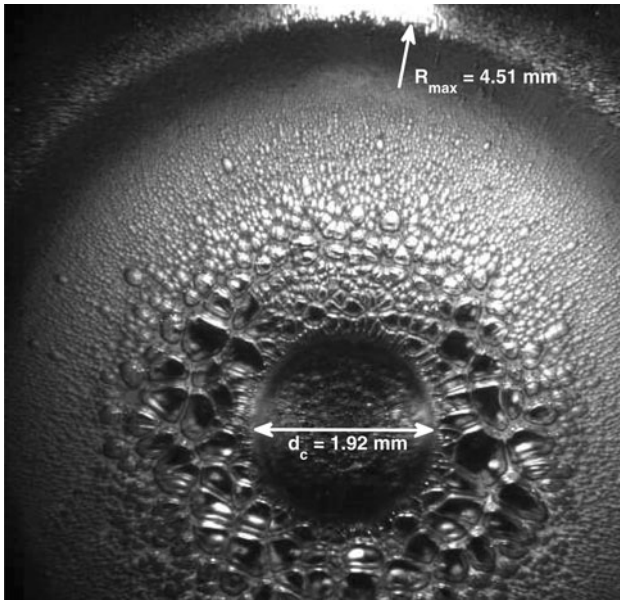


**Fig. 5** Detailed image from cavitation sequence in Fig. 4, taken at 1.4 ms after  $t_0$ . The central contact area is measured to be 1.92 mm in diameter and the maximum radius of the total cavitation structure is 4.51 mm.  $D = 38$  mm,  $\mu_0 = 12.13$  Pa.s,  $\delta = 1.5$  mm and  $u_i = 1.33$  m/s ( $St = 3.67$ ,  $\epsilon = 3.2 \times 10^{-5}$ )

(see bottom left image). The structure for this instance also lacks the intricate foam structure seen for non-Newtonian liquids. On one hand, both fluid types (i.e. Newtonian and non-Newtonian) cavitate once a threshold velocity/pressure is breached so they behave qualitatively the same. On the other hand, the viscosity in the non-Newtonian fluids varies both temporally and spatially leading to a vastly different structure. This spatial-temporal viscosity distribution is the subject of current analysis and will be addressed in a future publication.

Figure 10 shows the sequence for an impact onto a layer of pure glycerol ( $\mu = 1.25$  Pa.s)—the lowest viscosity Newtonian liquid tested. In this sequence, the evolution of the cavitation structure occurs much more rapidly due to the lower viscosity with the entire process taking just 1.3 ms from inception to collapse. Note that when the structure collapses in this case, a bubble remains at the centre of the impact site; this is marked with an arrow in the final image. We believe that this is due to the process of vapour entering the cavity since the liquids are not degassed (Kuhl et al. 1994; Yang et al. 2006).

A striking observation for the Newtonian liquids was that of a filament structure shown in Fig. 11, whereby the discrete bubbles appear more elongated with sharper tips which occurred during the initial inception of cavitation for pure syrup (high viscosity,  $\mu = 32$  Pa.s). Here, these filaments appear to be directed towards the centre of the impact site. We propose that this observation could

possibly be linked to the ‘glass-transition’ described by Donahue et al. (2010) as this was not seen for any other liquids. In contrast, Fig. 12 for 90% syrup ( $\mu = 1.6$  Pa.s) shows a snapshot whereby fractal-like filaments are shown to extend radially outward from the ‘contact radius’. Due to the timescale at which these filaments appear and the fact that they disappear rapidly, their origin is not yet fully understood and will require higher frame rate imaging which was not possible here due to limited illumination. This observation is subject to ongoing investigation.

### 3.3 Bubble size distributions

To highlight the qualitative difference in the appearance of the cavitation structure between Newtonian and non-Newtonian liquids, Fig. 13 shows examples of the bubble size distributions for Figs. 5, 8a and 9 all examined at the maximum extent of the cavitation structure. Only the measurable bubbles we examined which amounted to 202, 184 and 59 bubbles respectively. The data points indicate bubble diameters plotted against the radial distance of the bubble centre.

Since the bubbles are largely non-spherical, the projected bubble sizes shown are calculated by  $d_b = \sqrt{d_h d_v}$  where  $d_h$  and  $d_v$  are the horizontal and vertical extents (in the 2-D focal plane) of the bubbles respectively. Note that the non-spherical appearance close to the contact radius may eventuate from the dense packing whereby the bubbles can deform each other as with typical foam structures.

The data clearly shows the qualitative difference between the liquids; Fig. 13a ( $\mu_0 = 12.13$  Pa.s) and b ( $\mu_0 = 97.7$  Pa.s) for the non-Newtonian liquids show that the bubbles immediately surrounding the contact radius are quite fine with diameters  $d_b \sim 100$   $\mu\text{m}$  and increase rapidly to  $d_b \sim 600$   $\mu\text{m}$  at a radial distance from centre,  $r_s \sim 2$  mm. From these peaks, the bubbles then diminish with increasing radial distance up to  $r_s \sim 4$  mm after which, the bubble diameters are not measurable ( $d_b < 30$   $\mu\text{m}$ ). In contrast, the data for the Newtonian liquid (95% syrup,  $\mu = 8.47$  Pa.s) in Fig. 13c shows a completely different pattern; Here the bubble diameters grow linearly with increasing radial distance from  $d_b \approx 40$   $\mu\text{m}$  at  $r_s = 1.22$  mm to a maximum of  $d_b = 1,630$   $\mu\text{m}$  at  $r_s = 3.87$  mm. Note for  $r_b > 4.55$  mm in Fig. 13c, no bubbles are seen at all.

## 4 Contact diameter and maximum spread

As seen in Figs. 5, 6, 7, 8, 9 and 10, the cavitation structure extends from a centralised circle of finite radius which represents the area of the solids which deforms due to

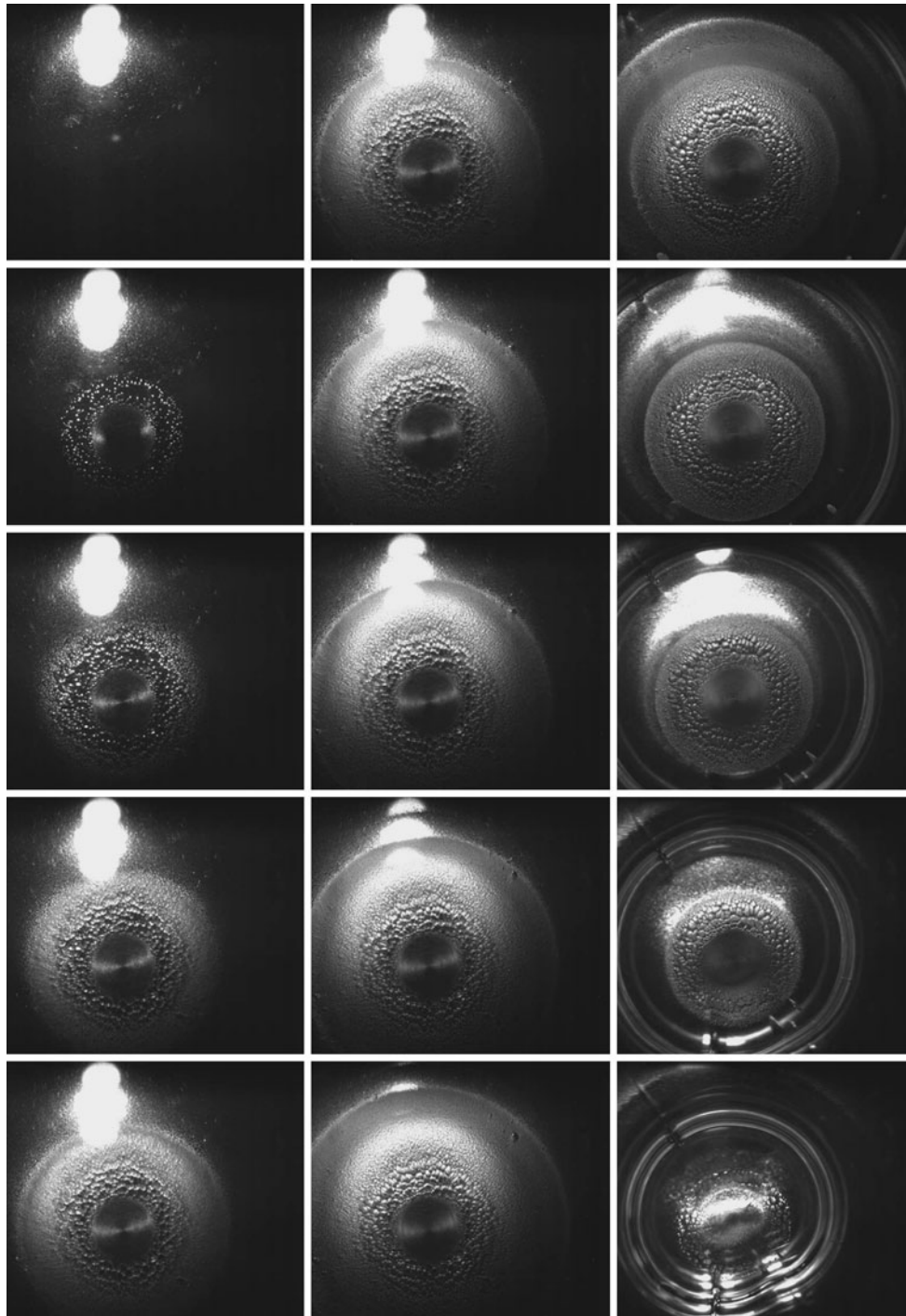


**Fig. 6** Cavitation pattern viewed from below. The *top left* image is the reference frame  $t_0$  before any cavitation bubbles are seen and subsequent frames (*top to bottom and left to right*) are taken at 0.1,

0.2, 0.3, 0.4, 0.5, 0.6, 0.7, 0.9, 1.4, 2.9, 3.9, 4.9, 5.9 and 7.9 ms after  $t_0$ .  $D = 38$  mm,  $\mu_0 = 58.2$  Pa.s,  $\delta = 1.5$  mm and  $u_i = 1.79$  m/s ( $St = 1.02$ ,  $\epsilon = 2.12 \times 10^{-4}$ )

elastic deformation. This contact diameter is readily obtained from the video clips for most liquid—sphere size combinations. Although solids deformation begins before the sphere reaches the minimum separation, this area only becomes visible when the sphere is close to the minimum separation and rebound due to the lighting in the

experimental setup and hence the observation coincides with the onset of cavitation in the video clips.

All raw data for the contact diameter ( $d_c$ ) is shown in Fig. 14, plotted against initial impact velocity upon entry into the layer ( $u_i$ ). Despite some scatter in the data, a monotonic increase in contact diameter with impact

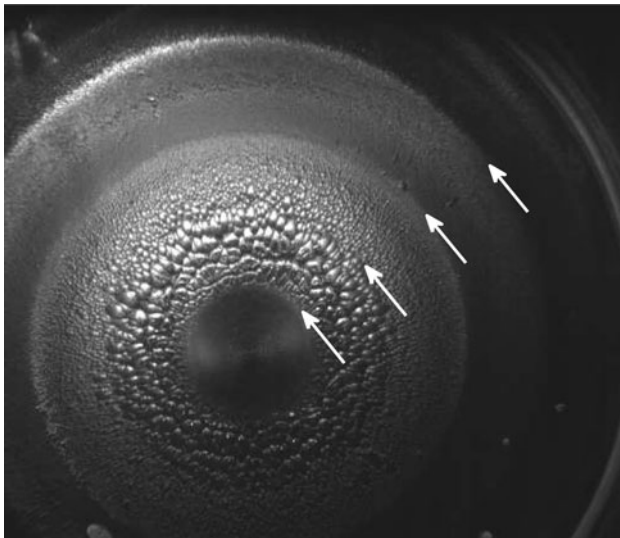


**Fig. 7** Detailed image from cavitation sequence in Fig. 6, taken at 2.9 ms from  $t_0$ . The central contact area is measured to be 2.1 mm in diameter and the maximum radius of the total cavitation structure is 5.7 mm.  $D = 38$  mm,  $\mu_0 = 58.2$  Pa.s,  $\delta = 1.5$  mm and  $u_i = 1.79$  m/s ( $St = 1.02$ ,  $\epsilon = 2.12 \times 10^{-4}$ )

velocity is generally observed for all liquid–sphere size combinations. This is to be expected since a higher impact velocity will result in stronger lubrication force acting on the nose of the sphere thus resulting in stronger deformation upon reaching the minimum separation. Following Davis et al. (2002), the instantaneous lubrication force can be given as

$$F_L(t) = 6\pi\mu a^2 v(t)/x(t), \quad (3)$$

where  $v(t)$  and  $x(t)$  are the instantaneous velocity of the sphere and separation respectively. At minimum separation,  $v(t) \sim v^*$  and  $x(t) \sim x_r$ , where  $v^*$  is a final, measurable velocity before motion is reversed and  $x_r$  is the elasticity lengthscale at which deformation is significant, given by Eq. 2.

At this stage it is worth noting that the surface roughness of the two approaching solids clearly can have a profound influence on the process. In the extreme case, such as that studied by Barnocky and Davis (1988) where 38  $\mu\text{m}$  roughness elements were simulated by fixing glass beads to a quartz surface, the minimum separation  $x_r$  is approximated by the roughness lengthscale  $x_b = 38 \mu\text{m}$ . This is likely to be several times higher than the typical roughness elements in the case studied herein using smooth glass and steel surfaces, where we expect the roughness to be  $O(10^{-6})$  m (Marston et al. 2010), but for high impact velocities and low viscosity liquids it is possible that the separation becomes comparable with the roughness lengthscale within the deformed region. For consistency, however, we use the approximation for  $x_r$ , given by Eq. 2 for these calculations.

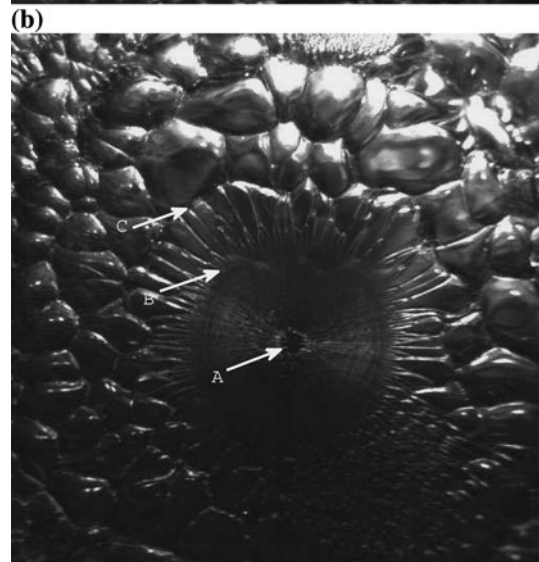
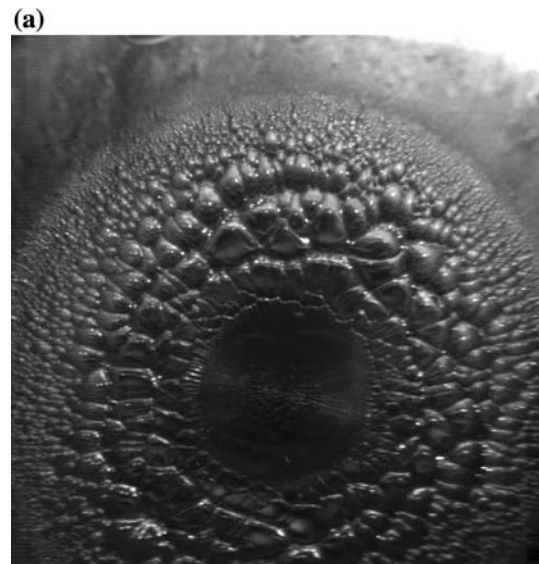


**Fig. 8** Example images from sequences taken using the Shin–Etsu silicone oils **a** taken at  $t = 3.45$  ms from  $t_0$  for  $D = 38$  mm,  $\mu_0 = 97.7$  Pa.s,  $\delta = 1.5$  mm and  $u_i = 1.79$  ( $St = 0.61$ ,  $\epsilon = 3.6 \times 10^{-4}$ ). See also the supplementary video for this figure. **b** Frame taken at  $t = 8.6$  ms from  $t_0$  for a  $D = 50$  mm,  $\mu_0 = 978$  Pa.s,  $\delta = 1.5$  mm and  $u_i = 1.5$  m/s ( $St = 0.067$ ,  $\epsilon = 4.5 \times 10^{-3}$ ). The contact area in this instance is 2.5 mm in diameter. The elongated bubble between arrows B and C has a length of 860  $\mu\text{m}$  and a width of 170  $\mu\text{m}$

Clearly, the choice of  $v^*$  is significant and whilst the approximation  $v^* = u_i/2$  may be used to achieve an analytical approximation, we can make a better approximation by tracking the motion of the sphere directly from the video frames allows us to determine the instantaneous velocity as a function of separation from the wall. Full details of this approach are given in Marston et al. (2010) where the apex (top edge) of the sphere is tracked using silhouette back-lighting with high magnification. As such, we calculate  $v^*$  as an average velocity over the last several frames, whilst

**Fig. 9** Sequence of images taken from a 10 kfps clip for a  $D = 50$  mm sphere impacting a glass base covered with a 1.5 mm layer of 95% golden syrup ( $\mu = 8.47$  Pa.s) with  $u_i = 1.5$  m/s ( $St = 7.72$ ,  $\epsilon = 3.9 \times 10^{-5}$ ). Viewed top to bottom and left to right, the top left image is the reference frame  $t_0$  and subsequent frames are taken at 0.1, 0.2, 0.4, 0.6, 0.9, 2.7, 3.3, 3.9, 4.5 and 5.1 ms after  $t_0$ . The left column shows the opening and the right column shows the collapse of the structure. The scale bar is 5 mm. See also the supplementary video for this figure

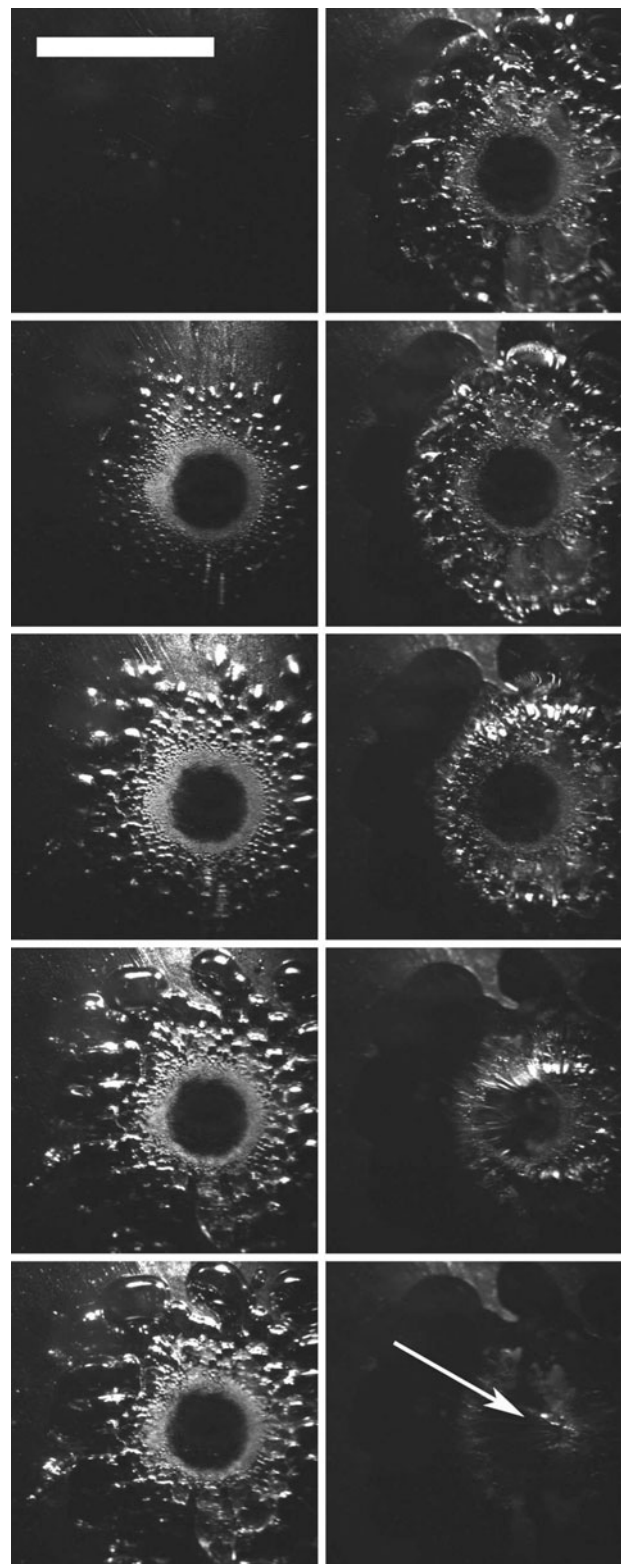
the velocity is still relatively uniform, that is before significant deceleration occurs and the direction of the sphere motion is reversed. An example of this approach is given in Fig. 15a showing the derivation of  $v^*$  (the close approach velocity) and  $u_r$  (the rebound velocity) for  $D = 38$  mm,  $\mu_0 = 12.13$  Pa.s and  $u_i = 0.83$  m/s. The symbols represent experimental data points derived from tracking the edge of the sphere during the penetration and rebound stages and the solid line indicate slopes representing our calculations of  $v^*$  and  $u_r$ , which for this realisation are 0.48 and 0.31 m/s respectively. Hence for this case,  $v^* = 0.58 u_i$ . Full results for a series of impact velocities determined by this method are plotted in Fig. 15b showing the monotonic increase in both  $v^*$  and  $u_r$  with increasing impact velocity. The ratio  $v^*/u_i = 0.13, 0.47, 0.58, 0.63, 0.65, 0.74, 0.82, 0.84$  for this fluid, which is expected as the shear rate diverges as the impact velocity increases implying a reduction in viscous dissipation compared with a Newtonian liquid with constant viscosity. The values of  $(v^*/u_i)^2$  also indicate how much energy is dissipated by the liquid during approach showing that as little as 30% up to 98% of the original kinetic energy of the sphere is dissipated during the travel through the liquid which, in turn may lead to localised liquid heating and hence viscosity reduction.

Using this approach, we deduce values of  $v^*$  for the range of liquids, sphere sizes and impact velocities used in Fig. 14 in order to calculate values of the lubrication force,  $F_L$ . Results for these calculation are shown in Fig. 16 where the data for the contact diameter from Fig. 14 is replotted against the lubrication force given by Eqs. 2 and 3. The data clearly shows an expected monotonic increase in  $d_c$  with increase in  $F_L$  and, by extrapolating the data, no contact diameter (i.e. no deformation) is expected below a threshold lubrication force of several hundred Newtons.

#### 4.1 Hertz contact theory

Following Landau and Lifshitz (1986), the flattened contact area can be compared to the Hertzian contact area. Thus, for the diameter of the contact area,  $d_c$ , we may write

$$d_c = \left( \frac{3DF}{E} \right)^{1/3}, \tag{4}$$



where  $D$  is the sphere diameter,  $F$  is the normal applied force and  $E$  is related to the Young's modulus and Poisson's ratio of the two solids by

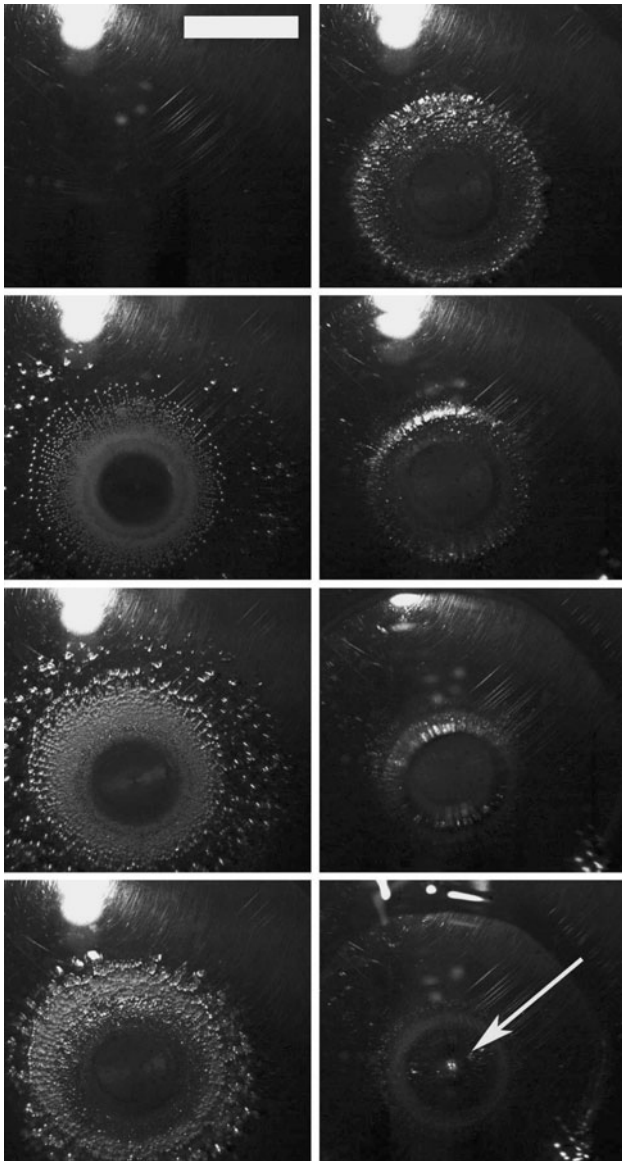


**Fig. 10** Cavitation evolution sequence for a  $D = 38$  mm sphere impacting onto a 1.5 mm layer of pure glycerol ( $\mu = 1.25$  Pa.s) with  $u_i = 1.5$  m/s ( $St = 39.7$ ,  $\epsilon = 3.82 \times 10^{-6}$ ). The frames shown from top to bottom and left to right are taken at 0, 0.2, 0.3, 0.5, 0.7, 0.9, 1.1, 1.3 ms from  $t_0$ . The arrow in the final frame indicates a vapour bubble remaining at the centre of the initial impact site. The scale bar is 5 mm

$$\frac{1}{E} = \frac{1 - \nu_1^2}{E_1} + \frac{1 - \nu_2^2}{E_2} \quad (5)$$

In static dry contact, the normal applied force is simply equated to  $F_{mg} = mg$ , where  $m$  is the mass of the sphere and  $g = 9.81 \text{ ms}^{-2}$  is the gravitational acceleration. However, for the case of a sphere impacting a thin, viscous layer, we must also include the lubrication force so that  $F = F_{mg} + F_L$ , where  $F_L$  is given by Eq. 3.

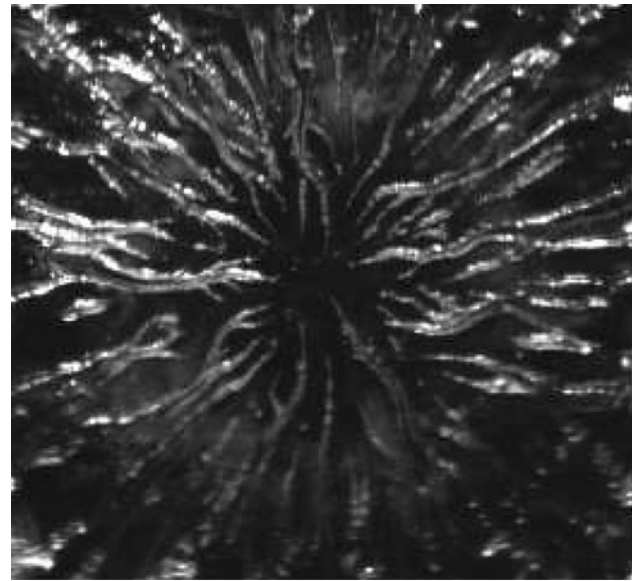


**Fig. 11** Snapshot of the filament structure during cavitation for a  $D = 50$  mm sphere impacting onto a 1.5 mm layer of pure syrup ( $\mu = 32$  Pa.s) with  $u_i = 2.4$  m/s ( $St = 3.27$ ,  $\epsilon = 2.36 \times 10^{-4}$ ). The frame shown is from a sequence taken at 20 kfps at 0.2 ms from  $t_0$



**Fig. 12** Filament-like structure at the onset of cavitation for a  $D = 38$  mm sphere impacting onto a 1.5 mm layer of 90% syrup mixture ( $\mu = 1.6$  Pa.s) with  $u_i = 1.79$  m/s ( $St = 37.1$ ,  $\epsilon = 5.84 \times 10^{-6}$ ). The frame shown is from a sequence taken at 20 kfps at 0.05 ms from  $t_0$

Order of magnitude estimates indeed show that the lubrication force expressed in Eq. 3 is dominant over capillary and gravitational forces during the close approach (Marston et al. 2010). Previous works by Lian et al. (1996, 2001) presented a closed-form approximation to the elasto-hydrodynamic problem for Newtonian and power-law fluids. Here, however, Eqs. 3–5 form an (uncoupled) approximate model which can be tested against the experimental values. Full results for this procedure are shown in Fig. 17a–c; symbols show experimental data

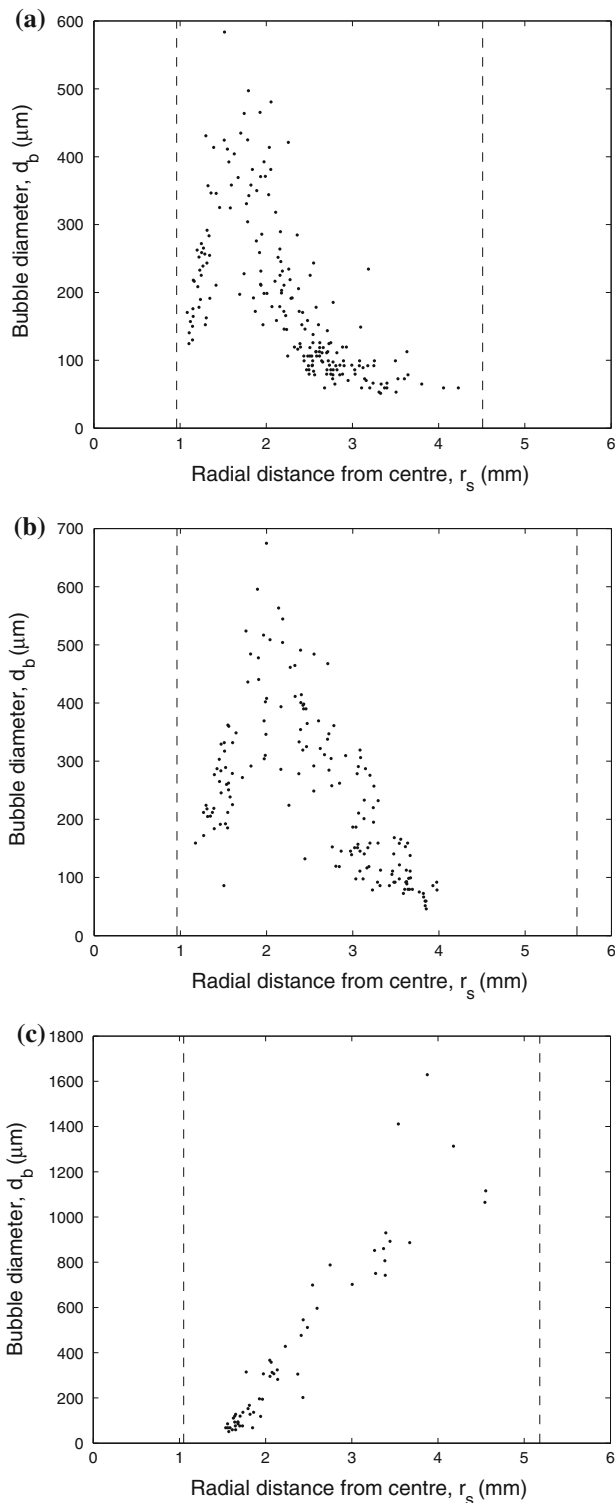


**Fig. 13** Bubble size distributions as a function of radial distance from the centre of impact for structures at maximum extent from **a** Fig. 5— $D = 38$  mm,  $\mu_0 = 12.13$  Pa.s,  $u_i = 1.33$  m/s, *non-Newtonian silicone oil*; **b** Fig. 8a— $D = 38$  mm,  $\mu_0 = 97.7$  Pa.s,  $u_i = 1.79$  m/s, *non-Newtonian silicone oil*; **c** Fig. 9— $D = 50$  mm,  $\mu = 8.47$  Pa.s,  $u_i = 1.5$  m/s, *Newtonian syrup*. The vertical dashed lines in each case denotes the radius from which the cavitation structure extends and the maximum extent of the overall structure respectively

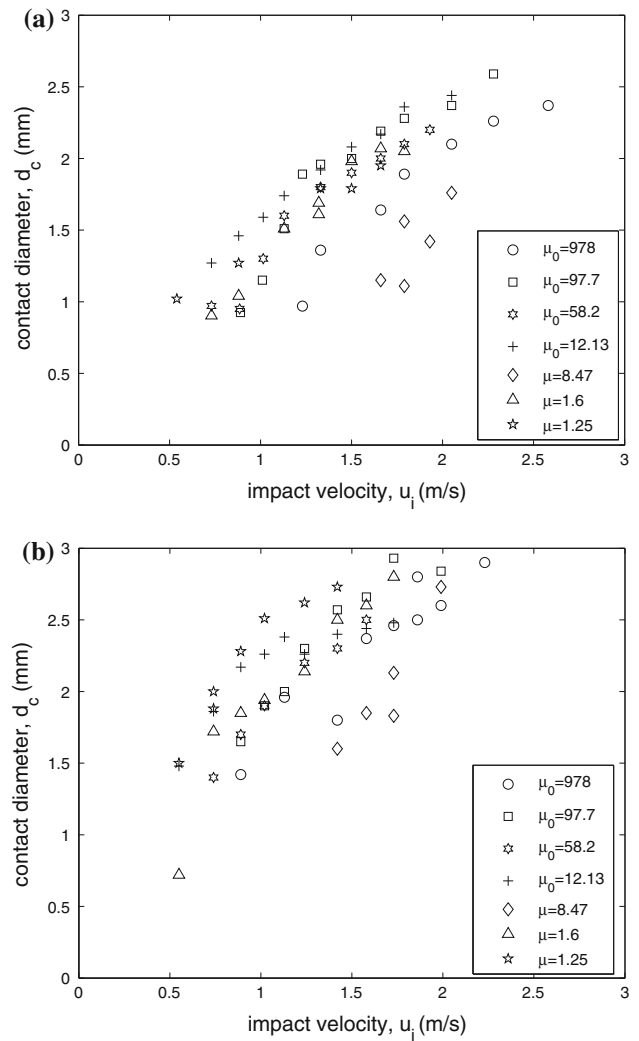


**Fig. 14** Plots of contact diameter,  $d_c$ , against initial impact velocity,  $u_i$  for **a**  $D = 38$  mm and **b**  $D = 50$  mm

plotted along with theoretical curves derived from Eqs. 3–5. The model clearly provides a quantitative agreement with the experimental data, however, it does not accurately describe the trends seen in most of the experiments. A description of the shear-thinning effect of the oils (e.g. Lian et al. 2001) and improved resolution of separation measurements may improve this model and will be addressed in the future. In addition, the effect of liquid compressibility and shear-thinning are difficult to compensate for, however, we estimate equivalent Newtonian viscosities for the highly non-Newtonian silicone oils based on effective shear rates upon approach to the wall. For example, in Fig. 8a for silicone oil with  $\mu_0 = 97.7$  Pa.s, we know that the sphere maintains a significant fraction of its velocity,  $u(t)$ , having slowed to 0.7 m/s at a gap widths,  $x(t) < 100$   $\mu\text{m}$ , nearing 10  $\mu\text{m}$ . Thus, a first approximation of the shear rate in this instance,  $\dot{\gamma} \sim u(t)/x(t) = 7 \times 10^4 \text{ s}^{-1}$ , yielding an equivalent viscosity of just 3 Pa.s based on the data in Fig. 2 and the

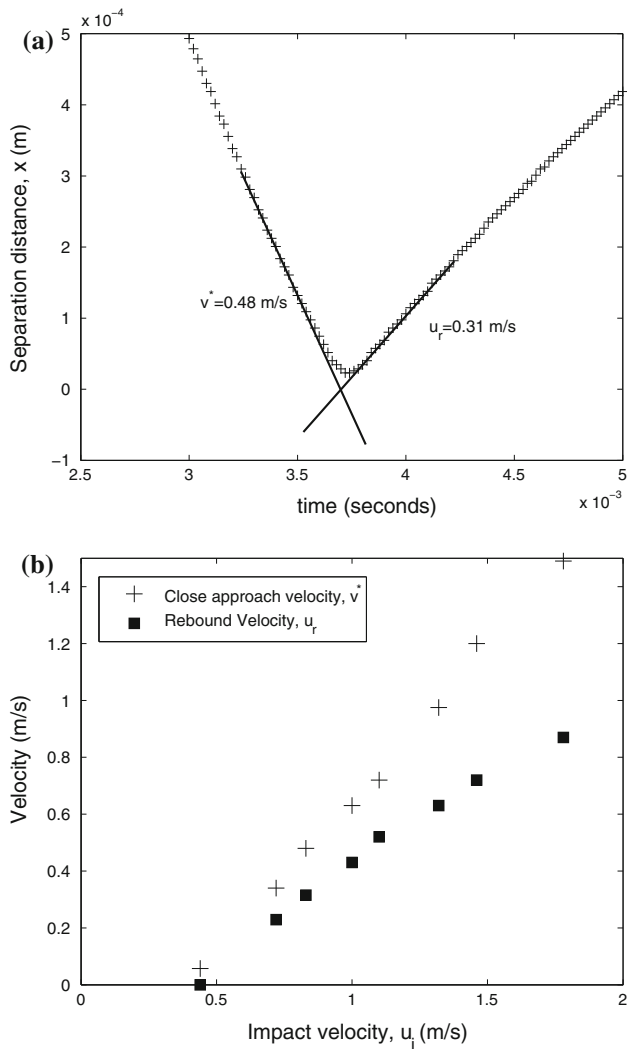


**Fig. 15** **a** Example of determination of close approach velocity,  $v^*$ , and rebound velocity,  $u_r$  for  $D = 38$  mm,  $\mu_0 = 12.13$  Pa.s,  $u_i = 0.83$  m/s (see main text for details of the derivation). **b** Full results for  $v^*$  and  $u_r$  for a series of impact velocities for  $D = 38$  mm and  $\mu_0 = 12.13$  Pa.s

Carreau model fit. A similar analysis is repeated for each individual case for all the silicone oils to extract an equivalent viscosity. The results of this approach indicate that we are likely to be underestimating the shearing rate in the thin layer for the higher impact velocities and shows the need for a more rigorous treatment of this effect in the present model. We also note that non-Newtonian effects are likely to be significant (Lian et al. 2001) and incorporating this is subject of ongoing work.

#### 4.2 Maximum spread and collapse of the cavitation structure

The high-speed images also allow us to directly measure the spread of the cavitation pattern itself (i.e. the maximum

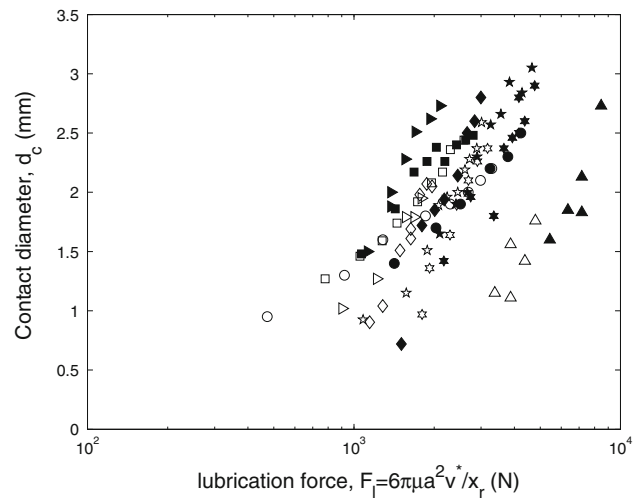


**Fig. 16** Plot of contact diameter,  $d_c$ , against the lubrication force,  $F_l = 6\pi\mu a^2 v^*/x_r$ . Data for  $D = 38$  mm are shown by open symbols,  $D = 50$  mm are shown by filled symbols

diameter of the total cavitation structure). See Fig. 5 for an example of the structure at maximum spread, just as the retraction towards the central impact site begins.

Figure 18a and b show the raw data for the maximum spread ( $r_{max}$ ) plotted against the initial impact velocity,  $u_i$ . Again, as expected, there is a general monotonic increase in  $r_{max}$  with  $u_i$  with one exception—for glycerol with  $D = 50$  mm (see Fig. 18b) where the spread appears to have reached a consistent level,  $r_{max} \sim 4$  mm. The independence of impact velocity for glycerol with  $D = 50$  mm indicates that the stress has reached a threshold level even for the lowest impact velocity. The increase in  $r_{max}$  for other liquids is also rather small compared to that observed for the non-Newtonian oils (97.7 and 978 Pa.s silicone oils) for both sphere sizes. In particular, for  $\mu_0 = 978$  Pa.s oil and  $D = 50$  mm, the radial spread increases from 5.1 mm at  $u_i = 0.89$  m/s to 10.9 mm at  $u_i = 2.23$  m/s; Similarly for  $\mu = 97.7$  Pa.s oil and  $D = 50$  mm,  $r_{max}$  increases from 3.3 to 9.23 mm for the same increase in  $u_i$ . The fact that the maximum spreading for non-Newtonian liquids exhibit a stronger dependence on the impact velocity is certainly related to their shear-thinning properties and may also be influenced by compressibility; as  $u_i$  increases, the liquid compresses more which reduces the separation and in turn influences the shear-thinning effect in the fluid layer separating the surfaces.

The presence of a clear radius, marking the boundary of the void structure is due to a combined effect of the weakened influence of the tensile stress in the liquid further away from the contact area and the hydrodynamic pressure of liquid returning into the area between the sphere and the wall.

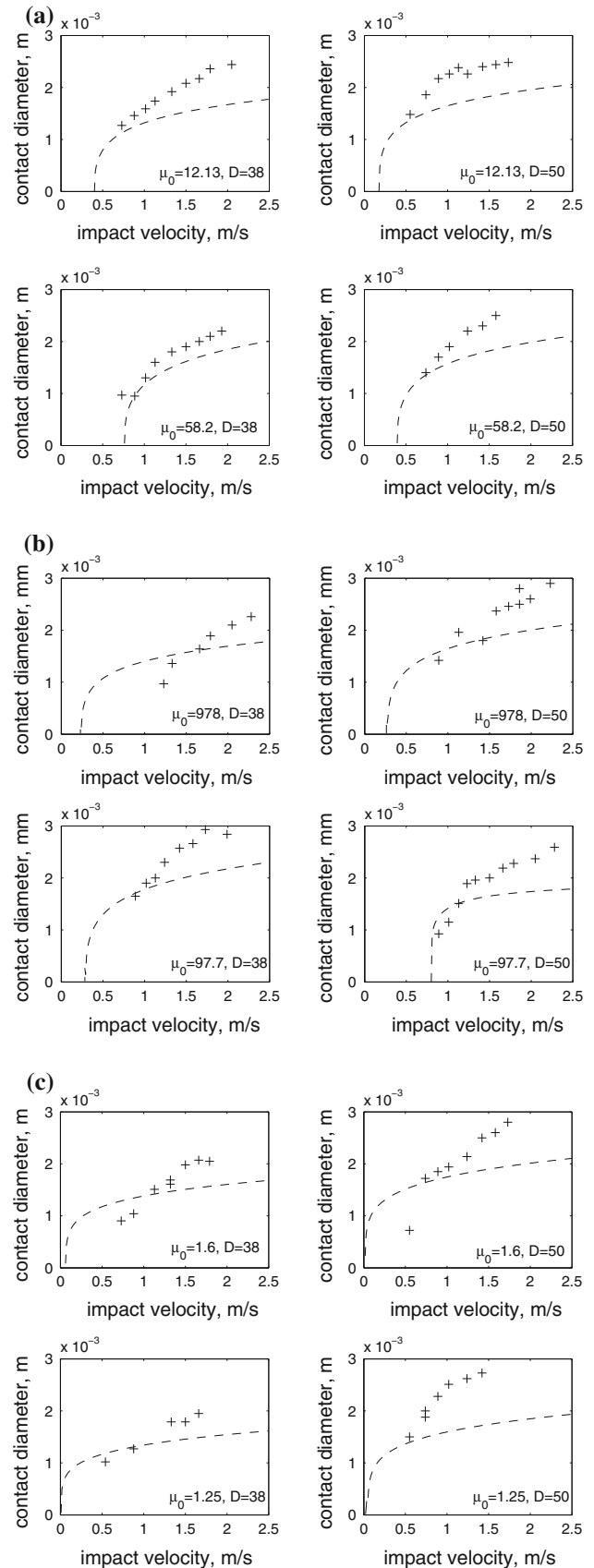
**Fig. 17** Data for the diameter of the central contact area plotted as a function of initial impact velocity. The *dashed curves* represent the modified Hertz contact theory from Eqs. 3–5, where  $v^*$  is derived from direct tracking of the motion of the sphere through the thin film. The plots shown are for **a** Brookfield silicone oils (non-Newtonian), **b** Shin-Etsu silicone oils (non-Newtonian) and **c** Syrup and glycerol (Newtonian). The legends indicate viscosity in Pa.s or low-shear viscosity ( $\mu_0$ ) in Pa.s for non-Newtonian liquids and sphere diameters in mm

From the theory of Davis et al. (1986), we can estimate the radial pressure distribution throughout the fluid at the instant of rebound with the following equation

$$P(r) = \frac{3\mu au_r}{(x_r + r^2/2a)^2} \quad (6)$$

where  $r$  is the radial coordinate. Using analysis similar to that shown in Fig. 15 for the close approach velocities,  $v^*$ , and rebound velocities,  $u_r$ , we can calculate values of the minimum separation as  $x_r = (6\pi\theta\mu a^3/2v^*/\sqrt{2})^{2/5}$ . An example of this approach is shown in Fig. 19a for the experimental conditions of Fig. 5 with  $v^* = 0.975$  m/s,  $x_r = 2.3 \times 10^{-5}$  m,  $u_r = 0.63$  m/s and  $\mu_0 = 12.13$ . Also shown in this plot is the equivalent distribution based on a corrected viscosity of  $\mu_{\text{eff}} = 3$  Pa.s accounting for shear-thinning with corresponding minimum separation of  $x_r = 1.12 \times 10^{-5}$ . The dashed line indicates atmospheric pressure, so that for radial locations above the line, cavitation can be expected. The modified theory, accounting for shear-thinning indicates that the cavitation should extend to a radius of 5.6 mm, in reasonable agreement with the experimental value of 4.5 mm in Fig. 5. Applying this analysis over the range of impact velocities used for this fluid yields the data presented in Fig. 19b where it can be seen that the theory consistently over-estimates the extent of the cavitation structure but captures the qualitative trend seen in the experimental measurements. Note that we analyse the bulk of the data in terms of the maximum tension criterion (discussed in the next section) as using the threshold of  $P_r < 100,000$  N/m<sup>2</sup> is essentially equivalent to this.

One striking difference between Newtonian and non-Newtonian liquids was noted during the collapse of the cavitation structure. For Newtonian liquids, the radius of cavitation reaches a clear maximum and then collapses towards the centre as the liquid returns towards the impact site (see e.g. Figs. 9, 10). Figure 20a shows data for the collapse of the structure for several realisations with Newtonian liquids. Here, the time to reach maximum extent decreases and the rate of collapse increases with increasing impact Stokes' number, as one might expect since this quantity represents the ratio of sphere inertia to viscous forces thus a lower Stokes' number indicates a



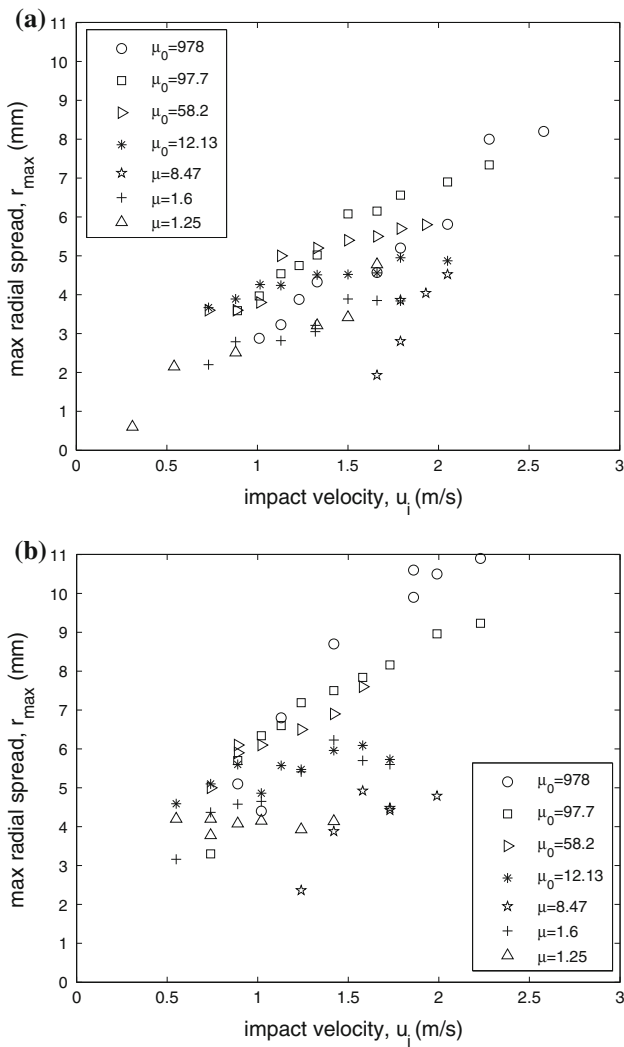


**Fig. 18** Plots of maximum radial spread of the cavitation structure,  $r_{\max}$ , against initial impact velocity,  $u_i$  for **a**  $D = 38$  mm and **b**  $D = 50$  mm

weaker viscous force. In contrast, the highest viscosity silicone oils did not always collapse—see for example, Fig. 8b where the structure remains stable for some time after the maximum extent was reached. In Fig. 19b we present examples of the collapse for such cases. As seen in the data, the radius of the structure does not decay as rapidly as seen in the Newtonian case and, in fact, does not diminish over the time of the recordings. With reference to Figs. 1c and 8b, we believe that this is due to the fact that the liquid bridge between the plate and the sphere “snaps” so that there is no pressure driving the liquid to return to the impact site and the “ceiling” of the cavitation bubbles collapse at their current radial location. As such, the snapping of the liquid bridge marks a transition in the collapse and an example of where this transition occurs in the radius versus time curves is marked in Fig. 19b.

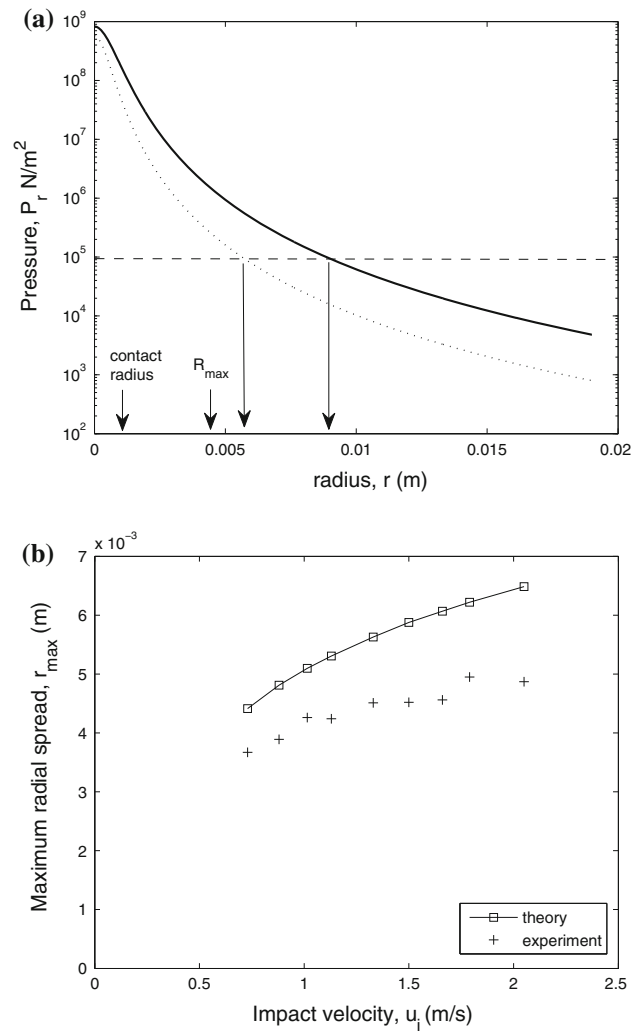


**Fig. 19 a** Radial pressure distribution in the liquid film for the experimental conditions of Fig. 5. The *solid line* plots the pressure for  $\mu_0 = 12.13$  Pa.s with corresponding minimum separation  $x_r = 23$   $\mu\text{m}$  whilst the *dotted line* plots the pressure with effective viscosity  $\mu_{\text{eff}} = 3$  Pa.s and  $x_r = 11$   $\mu\text{m}$ . The *horizontal dashed line* at  $P_r = 10^5$   $\text{N/m}^2$  is atmospheric pressure. **b** Experimental measurements vs. predicted measurement for the maximum extent of the cavitation structure for  $\mu_0 = 12.13$  and  $u_i = 0.73$ – $2.05$  m/s ( $St = 1.99$ – $5.6$ )

### 5 The maximum tension criterion: comparison with experiments

For a liquid devoid of dissolved gas or other possible inception sites for nucleation, the cavitation criterion depends on the tensile strength of the liquid (e.g. Williams and Williams 2002). However, since the liquids used in this study were used as supplied from the manufacturer in contact with the ambient atmosphere, this criterion can not be applied and we instead invoke a criterion based on the tensile *stress* in the liquid—Joseph (1998) states an approximate criterion for the occurrence of cavitation based

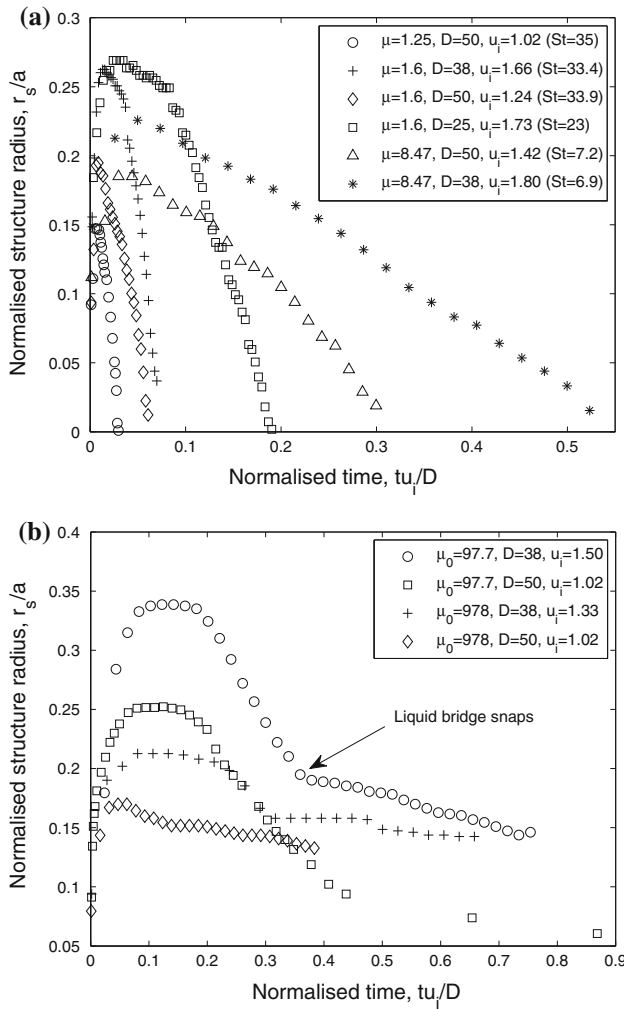


**Fig. 20** Plots of the cavitation structure radius versus time for **a** Newtonian and **b** non-Newtonian liquids. Radii have been normalised with respect to the sphere radius and time with respect to the natural timescale  $D/u_i$

on the tensile stress in the liquid due to the separation of two surfaces. This stress is given by

$$T \sim 2\mu\dot{S} \tag{7}$$

where the rate of strain,  $\dot{S}$  is estimated here by  $u_r/x_{\min}$  where  $u_r$  is the rebound velocity of the sphere (well defined about 10  $\mu\text{s}$  after the reversal of motion) and  $x_{\min}$  is the minimum distance separating the nose of the sphere and the surface of the glass plate. If this stress exceeds one atmosphere of pressure, cavitation is to be expected according to the maximum tension criterion. Thus, we must know the separation and velocity of the spheres at the moment of rebound (i.e. the point at which the direction of motion of the sphere is reversed).

Again, tracking the sphere motion through the liquid layer provides a first approximation to the rebound

**Table 2** Parameters used in calculation of liquid tensile stress showing that  $T > 1$  for all the examples presented in Figs. 3, 4, 5, 6, 7, 8, 9, 10 and 11, thus cavitation is expected in all cases by the maximum tension criterion

Figure number	$\mu$ (Pa.s)	$u_r$ (m/s)	$x_r$ ( $\mu\text{m}$ )	$T$ (atm)
4 and 5	$\sim 2$	0.63	9.7	2.6
6 and 7	$\sim 3$	0.77	12.9	3.6
8a	3	0.3	11.9	1.5
8b	5	0.3	12.3	2.4
9	8.47	0.21	16.8	2.1
10	1.25	0.6	8.4	1.8
11	32	0.39	29	8.5
12	1.6	0.9	9.8	2.9

Note values of  $T$  are stated in atmospheres (1 atm =  $10^5$  Pa)

velocity,  $u_r$ . We make use of the elasticity lengthscale,  $x_r = (6\pi\theta\mu\alpha^{3/2}v^*/\sqrt{2})^{2/5}$  for the minimum separation, so that  $x_{\min} \sim x_r$ . Note for most Newtonian liquids with  $\mu > 0.1$  Pa.s and moderate sphere impact velocities ( $u_i \sim 1$  m/s),  $x_r \approx 1\text{--}10$   $\mu\text{m}$ .

In practice, of course, the observed rebound velocity itself will depend on the liquid viscosity, the film thickness and the initial impact velocity. However, we may use Eq. 7 to compare to experimental data for the onset and spread of the cavitation, i.e. the critical conditions associated with the first observation of cavitation.

For Newtonian liquids this comparison is straightforward. For Fig. 9 ( $\mu = 8.47$  Pa.s), the velocity of the sphere close to the wall (from tracking experiments) is 0.97 m/s, the minimum separation reached, approximated by  $x_r$ , is 16.8  $\mu\text{m}$  and the rebound velocity is 0.21 m/s. Thus, we find  $T \sim 2.1 \times 10^5$  Pa, which exceeds 1 atmosphere of pressure and hence cavitation is expected. For non-Newtonian liquids we must first approximate a viscosity using the approach detailed in Sect. 4.1.

In Table 2, we list the parameters used in, and calculation of, the stress given by Eq. 7 for Figs. 5, 6, 7, 8, 9, 10, 11 and 12. The stated values of  $x_r$  for Figs. 5, 6, 7 and 8 are likely to be over-estimates due to the effect of liquid compressibility. This would inevitably lead to smaller gap widths, higher values of effective shear rates and lower viscosities. As such, the values of  $T$  are considered underestimates for these fluids. Nonetheless, we find that the maximum tension criterion correctly predicts the occurrence of cavitation for all the examples presented in Figs. 5, 6, 7, 8, 9, 10, 11 and 12. Note that the values of  $T$  are calculated at the point of minimum separation and thus only valid at this point. The fact that the cavitation patterns are seen over several frames in the video sequences may be due to the effect of dissolved gases entering the cavity which is initially a vacuum, as proposed by Kuhl et al. (1994).

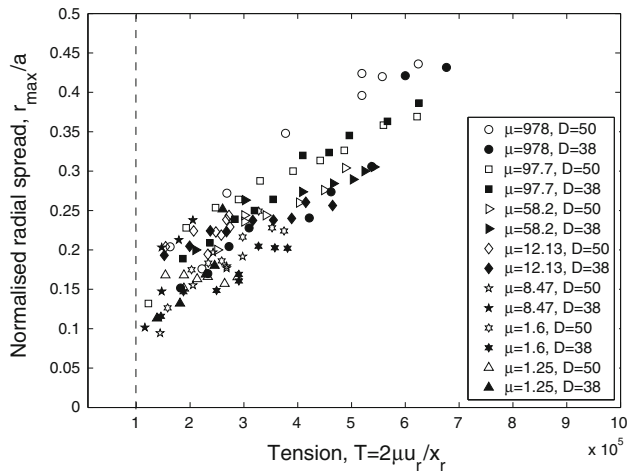


**Fig. 21** Normalised maximum spread,  $r_{\max}/a$ , of the cavitation structure plotted against the tensile stress,  $T \sim 2\mu u_r/x_r$ . Data for  $D = 38$  mm shown by filled data points,  $D = 50$  mm shown by open data points. The vertical dashed line indicates the threshold  $T_c = 1$  atm

Since the stress in Eq. 7 governs the onset of the cavitation, it is natural that the extent of the cavitation structure should also scale with stress. This is clearly the case when the data for the normalised maximum spread in Fig. 18a and b is replotted against the stress, as shown in Fig. 21. Here, the threshold stress  $T_c = 1$  atm is marked by the vertical dashed line and we see that  $r_{\max}$  increases from a minimum of  $0.05 D$  at  $T = T_c$  to  $0.22D$  at  $T = 6.76$ . Whether this trend continues indefinitely or reaches a maximum could not be determined from this study due to limitations on impact velocity. However, we expect that as the sphere moves further away from the surface, the tensile stress decreases (since  $T \sim x^{-1}$ ) and will eventually fall back below the threshold  $T_c = 1$  atm whereby the fluid squeezed out during impact returns, thus providing a physical limit to the extent of the cavitation.

### 6 Conclusions

A novel cavitation structure has been observed using high-speed video imaging. The cavitation was observed during the elastohydrodynamic rebound of solid spheres from a solid planar surface and initiated at the instance of reversal of the direction of motion. Using estimates of the tensile stress in the liquid we expect cavitation to occur due to the large viscosity used and small gap widths achieved during penetration and our experimental observations coincide with the idea that the fluid will cavitate once this tensile stress exceeds one atmosphere of pressure.

We have verified that an area around the tip of the impacting sphere becomes deformed due to the high

lubrication force and modelled this feature using a modified form of Hertz contact theory.

We discovered stark differences between the qualitative features of the cavitation bubble structures for Newtonian and non-Newtonian liquids. Both cases exhibit discrete rings of bubbles growing radially outward from the site of impact. However, in the Newtonian case, the bubbles increase in size and are more discrete whereas for the non-Newtonian liquids we observe rings of large bubbles followed by rings of smaller bubbles connected in a foam-like structure. The fact that the foam-like structure of the cavitation is so pronounced and intricate for these non-Newtonian liquids is clearly due to the nature of the fluid, similar to the observations of Seddon and Mullin (2008) who observed “tongues of fluid” stretched across the cavitation site for a visco-elastic fluid for a steady cavitation bubble under a rolling sphere. The long molecular chains are likely to be the cause of the complex patterns and may help to stabilise the structure once vapour enters the cavities.

This fundamental observation may provide a new criterion for testing the short-time dynamical nature of a liquid.

Extensions to this work may consider more exotic non-Newtonian liquids in order to better characterise the influence of the nature of the fluid. Also, experiments performed at varying ambient pressures would help to provide a more rigorous examination of the maximum tension criterion. The fact that none of the liquids used herein were degassed may have also benefitted the radial extent of the cavitation structures as noted by Yang et al. (2006) and hence reinforce the need for repeat experiments under reduced ambient pressures to provide insight into this influence.

**Acknowledgments** This work was initiated while W. Yong was attached to ICES from NUS during an undergraduate industrial attachment scheme under J.O. Marston. The work was supported by the Science and Engineering Research Council of A\*STAR (Agency for Science, Technology and Research), Singapore. The authors would like to thank Ng Junwei for technical support and Professors T.G. Etoh & K. Takehara at Kinki University for use of their laboratory for some early experiments in this work.

### References

Ardekani AM, Joseph DD, Dunn-Rankin D, Rangel RH (2009) Particle-wall collision in a viscoelastic fluid. *J Fluid Mech* 633:475–483

Ashmore J, Del Pino C, Mullin T (2005) Cavitation in a lubrication flow between a moving sphere and a boundary. *Phys Rev Lett* 94:124501

Barnocky G, Davis RH (1988) Elastohydrodynamic collision and rebound of spheres—experimental verification. *Phys Fluids* 31:1324–1329

- Davis RH, Serayssol J-M, Hinch EJ (1986) The elastohydrodynamic collision of two spheres. *J Fluid Mech* 163:479–497
- Davis RH, Rager DA, Good BT (2002) Elastohydrodynamic rebound of spheres from coated surfaces. *J Fluid Mech* 468:107–119
- Donahue CM, Hrenya CM, Davis RH, Nakagawa KJ, Zelinskaya AP, Joseph GG (2010) Stokes' cradle: normal three-body collisions between wetted particles. *J Fluid Mech* 650:479–504
- Joseph DD (1998) Cavitation and the state of stress in a flowing liquid. *J Fluid Mech* 366:367–378
- Kantak AA, Davis RH (2004) Oblique collisions and rebound of spheres from a wetted surface. *J Fluid Mech* 509:63–81
- Kantak AA, Hrenya CM, Davies RH (2009) Initial rates of aggregation for dilute, granular flows of wet (cohesive) particles. *Phys Fluids* 21:023301
- Kuhl T, Ruths M, Chen Y, Israelachvili (1994) J. Direct visualisation of cavitation and damage in ultrathin liquid films. *J Heart Valve Dis* 3(suppl. 1):117–127
- Landau LD, Lifshitz EM (1986) *Theory of elasticity*, 3rd edn. Butterworth-Heinemann, Oxford
- Lian G, Adams MJ, Thornton C (1996) Elastohydrodynamic collisions of soft spheres. *J Fluid Mech* 311:141–152
- Lian G, Xu Y, Huang W, Adams MJ (2001) On the squeeze flow of a power-law fluid between rigid spheres. *J Non-Newton Fluid Mech* 100:151–164
- Marston JO, Yong W, Thoroddsen ST (2010) Direct verification of the lubrication force on a sphere travelling through a viscous film upon approach to a solid wall. *J Fluid Mech* 655:515–526
- Prokunin AN, Slavin RV (2006) Cavitation-induced particle-wall interactions in Newtonian and non-Newtonian fluids. *Rheol Acta* 45:348
- Salman AD, Hounslow MJ, Seville JPK (eds) (2006) *Handbook of powder technology*, vol11: granulation. Elsevier, Amsterdam
- Seddon JRT, Mullin T (2008) Cavitation in anisotropic fluids. *Phys Fluids* 20:023102
- Williams PR, Williams RL (2002) Cavitation of liquids under dynamic stressing by pulses of tension. *J Phys D Appl Phys* 35:2222–2230
- Yang L, Seddon JRT, Mullin T, Del Pino C, Ashmore J (2006) The motion of a rough particle in a Stokes flow adjacent to a boundary. *J Fluid Mech* 557:337–346